Deep-Sea Research I 99 (2015) 75–86

Contents lists available at ScienceDirect

Deep-Sea Research I

journal homepage: www.elsevier.com/locate/dsri

Settling of particles in the upper 100 m of the ocean detected with autonomous profiling floats off California

George A. Jackson [a,*], David M. Checkley Jr.[b], Michael Dagg [c]

[a] Texas A&M University, College Station, TX 77843, USA
[b] Scripps Institution of Oceanography, University of California, San Diego, La Jolla, CA 92093, USA
[c] Louisiana Universities Marine Consortium, 8124 Highway 56, Chauvin, LA 70344, USA

ARTICLE INFO

Article history:
Received 24 October 2014
Received in revised form
23 January 2015
Accepted 1 February 2015
Available online 7 February 2015

Keywords:
SOLOPC
Particle settling
In situ settling velocities
Aggregates
Particle flux

ABSTRACT

We have deployed an autonomous profiling float, the SOLOPC, to sample the concentration of particles larger than 100 μm off the California coast at approximately hourly intervals down to at least 100 m for periods as long as 12 d. We used the data to estimate total aggregate concentrations hourly at 2-m depth intervals, studying the dynamics of particle sedimentation in this difficult-to-sample region. We find that even over time scales of a week, sedimentation is highly variable, with detectable sedimentation events on about one quarter of the days. Most of these observations were along the southwest coast of the United States, a region known for its coastal upwelling and not necessarily representative of more oligotrophic regions. The aggregate settling rates that we estimate, on the order of 50 m d^{-1}, are consistent with in situ measurements and with rates calculated from coagulation models. The time interval between observations and their vertical resolution constrain the velocities that can be measured. To capture particle settling with velocities less than the 100 m d^{-1} that is usually reported for near surface aggregates requires a sampling interval no more than about 0.25 d with a 2 m vertical resolution. This technique provides a powerful new tool to study the dynamics of particles and their sedimentation near the ocean surface, where export starts.

1. Introduction

Understanding the fate of organic matter produced in the ocean's surface layer is one of the enduring scientific problems with important consequences for how the ocean and planet respond to changes in global carbon dioxide concentrations. It involves a complex web of interacting biological and physical processes that produce, transform and consume falling particles. The relative importance of the processes varies with depth and with time. Observations in one region and time do not necessarily relate to those at different depths and times.

Much our understanding of the fluxes has been developed from the collection of material falling in sediment traps and its subsequent analysis. Limitations of sediment traps tend to favor their use at depths 300 m and greater (e.g., Buesseler et al., 2007). However, observations, encapsulated in the curve of Martin et al. (1987), show that at least 50% of losses of falling particle carbon occur within 100 m of the euphotic zone. This near-surface region is one of the least understood regions in the vertical flight of organic matter.

Trap deployments usually lack sufficient vertical resolution to resolve the changes occurring over depth differences of meters. Furthermore, there is a temporal aspect: traps typically integrate over too long a time to capture short-term events that we increasingly know are important to overall flux. There is a need for methods that characterize particle dynamics on short time and space scales near the ocean surface.

Profiling floats and gliders equipped with particle sensing proxies, including optical backscatter and inferred aggregate concentrations, have been used to observe the descent of particles in the North Atlantic (Briggs et al., 2011), the Norwegian Sea (Dall'Olmo and Mork, 2014), and in the North Pacific (Petrik et al., 2013). These estimates have relied on manual fitting of lines to depth and time plots of maximum particle concentrations.

While there have been numerous observations and analyses within the near-surface depth zone, there continues to be a need for new approaches in the study of particle flux. The marriage of a Laser Optical Particle Counter (LOPC) with a SOLO float to make the SOLOPC has provided a way to extend particle observations into the time domain (Checkley et al., 2008). The LOPC uses light absorbance by objects passing perpendicularly through a laser

* Corresponding author. Tel.: +1 979 845 0405.
E-mail addresses: gjackson@tamu.edu (G.A. Jackson), dcheckley@ucsd.edu (D.M. Checkley Jr.), mdagg@lumcon.edu (M. Dagg).

http://dx.doi.org/10.1016/j.dsr.2015.02.001

light sheet composed of the equivalent of 70 1 mm light beams to find and size the objects passing through (Herman et al., 2004). The LOPC is attached to the lower end of the SOLO float, so that it is on the leading edge of the float when it samples on its downward path (Checkley et al., 2008). CTD sensors are on the upper end of the float and sample on the upward path. The SOLOPC can provide the size-resolved concentrations of particles larger than 100 μm, with vertical distributions depth-resolved by as little as 2 m between the surface and 400 m and with measurements made at almost hourly intervals for 3 weeks or, at longer time intervals, for as long as a year. The potential for float collision with the bottom makes deployments in coastal regions riskier than further offshore.

Two types of particles have been believed to dominate the passive vertical flux. First are the fecal pellets formed by zooplankton after feeding on algae and other particles. Other forms of downward transport known to be important include colloids and dissolved organic matter (e.g., Dall'Olmo and Mork, 2014; Briggs et al., 2011). Despite their lower abundances, fecal pellets can be an important component of the flux because of their high densities and fast sinking speeds (e.g., Turner, 2014; Ploug et al., 2008). Fecal pellet flux at our Gatekeeper site (Table 1, Fig. 1) is the subject of a separate paper (Dagg et al., 2014).

The alternate sinking vehicles are the relatively amorphous aggregates, the largest known as "marine snow", that are formed by multiple processes bringing particles together and causing them to stick (e.g., Alldredge and Gotschalk, 1989; Jackson, 1995). Jackson and Checkley (2011) used SOLOPC observations to separate out zooplankton and aggregates in the particle field. This separation was extended in Petrik et al. (2013) by developing a technique for estimating the aggregate concentration from the particle size distributions. Note that the SOLOPC does not resolve the relatively rare fecal pellets (Dagg et al., 2014).

When analyzing the SOLOPC data, we have observed what appear to be settling events in the aggregate distributions (e.g., Petrik et al., 2013). In this paper, we develop statistical techniques to quantify these events and apply the methods to the SOLOPC data. We hypothesize that aggregates sink in events that can be observed in sequential profiles by the SOLOPC. We test this hypothesis using cross-correlations of aggregate concentrations at different time and depth separations. The motivation is that, as time separation used for the comparison increases, particles fall deeper. As a result, the highest correlations between concentrations at two different depths should shift to increased depth separations with increased time separations. Our results yield frequencies of settling events and average settling rates of aggregates. They document episodic aggregate escape from the euphotic zone by sinking. The techniques we develop are applicable to other observations.

2. Methods

Vertical profiles of particle size and abundance were collected with a SOLOPC profiling float (Checkley et al., 2008). The SOLOPC descends from the surface to a preset depth, sampling particle distributions on the way down, sending a subset of the data via an Iridium satellite when it returns to the surface. Besides measurements of particle abundance as a function of size and depth, other data collected by the SOLOPC include location and depth distributions of temperature and salinity, as well as backscatter and/or chlorophyll *a* fluorescence.

SOLOPC floats have been deployed off the coast of California in conditions that range from upwelling eutrophic to oligotrophic, as well as on one brief deployment in the North Atlantic. The deployments discussed here were in the central and southern California Current System (Checkley and Barth 2009). The California Current System is comprised of the southward-flowing California Current (salinity $\lesssim$33.2) offshore, a coastal region with periodic wind-driven upwelling (salinity $\gtrsim$33.2) and, in the winter, the northward-flowing Davidson Current, and the northward-flowing California Undercurrent. Wind-stress curl-driven upwelling often occurs between the coastal upwelling and California Current (Rykaczewski and Checkley, 2008). The Southern California Bight, south and east of Point Conception, has a cyclonic circulation and variable productivity. In general, coastal upwelling and flow of the California Current are greatest in spring and summer.

Here, we analyze the observations for deployments having a minimum of 27 profiles (Table 1). The SOLOPCs sampled from the surface to 100–200 m depth. To avoid contamination of the LOPC data with bubbles, we discarded particle data collected in the surface 2 m. The cycle time for each dive was typically about 1 h. Gatekeeper (GK1-6) deployments occurred in July 2010 in

Table 1
Deployment information. **Depl.** refers to the deployment number; **ID** is the deployment identification used in this paper; L**aunch date** is the date in local time for the deployment; **Launch lat.** and **long**. are the initial positions. The standard profile was beween 0 and 100 m.

Cruise	Depl.	ID	Launch date	Launch lat.	Launch long.	No. of dives	Deploy. duration (d)
Sproul05	1	Sp05	28-Sep-05	33.0°N	−118.0°E	63	2.79
NewHorizon06	1	NH06	14-Sep-06	34.3°N	−121.1°E	86	4.17
Thompson07	1	Th07-1	4-Apr-07	34.3°N	−120.9°E	70	3.88
	2	Th07-2	9-Apr-07	33.6°N	−123.1°E	72	3.46
	4	Th07-4	16-Apr-07	34.2°N	−121.2°E	76	4.13
Gatekeeper	1	GK-1	11-Jul-10	36.8°N	−122.1°E	41	1.83
	2	GK-2	14-Jul-10	37.0°N	−123.3°E	192	8.75
	3	GK-3	17-Jul-10	36.8°N	−122.1°E	31	1.38
	4[a]	GK-4	19-Jul-10	36.8°N	−122.0°E	8	0.38
	5	GK-5	20-July-10	36.8°N	−122.1°E	31	1.38
	6	GK-6	22-July-10	36.6°N	−122.1°E	27	1.21
NewHorizon1307	1[b]	NH13-1	18-Apr-13	33.0°N	−117.9°E	255	11.50
	2[c]	NH13-2	18-Apr-13	33.0°N	−117.9°E	252	12.29

[a] Data not used because of short deployment.
[b] The depth ranges for NH13-1 and -2 were adjusted during their deployments for operational reasons but were always to at least 78 m. The largest number of uninterrupted dives to 100 m were 148 and 160, and 177 and 160 to 200 m for NH13-1 and -2. Unless otherwise noted, the longer data set of profiles to 78 m was used for these two deployments.
[c] The depth ranges for NH13-1 and -2 were adjusted during their deployments for operational reasons but were always to at least 78 m. The largest number of uninterrupted dives to 100 m were 148 and 160, and 177 and 160 to 200 m for NH13-1 and -2. Unless otherwise noted, the longer data set of profiles to 78 m was used for these two deployments.

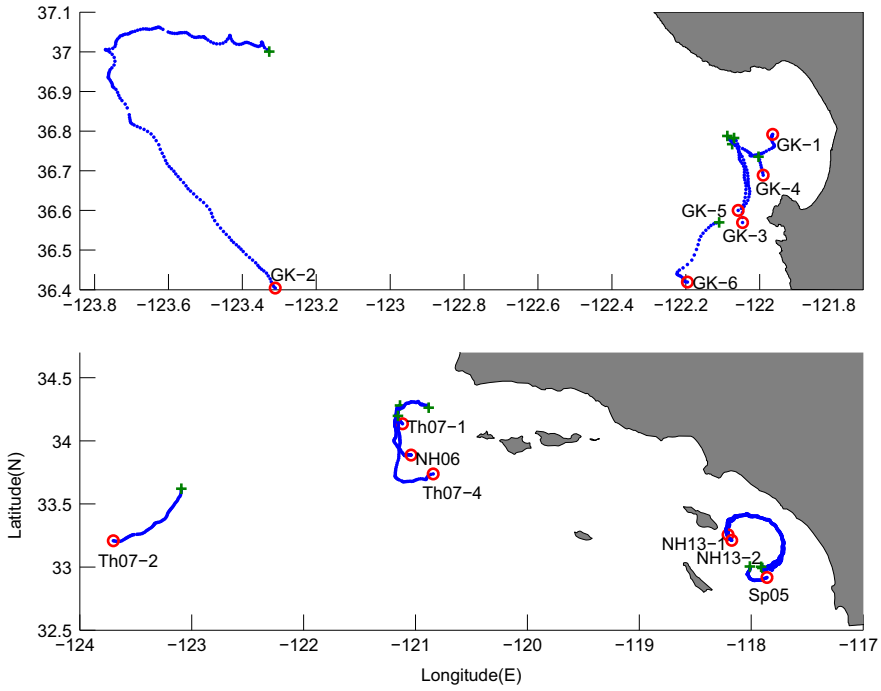

Fig. 1. Locations of deployments. Top: Gatekeeper cruise region, showing deployments GK-1 to GK-6 in Monterey Bay; bottom: deployments in Southern California. Green+and red o indicate launch and retrieval locations; blue dots indicate dive locations.

Monterey Bay (MB), which is, like other coastal areas, at times affected by upwelling (Breaker and Broenkow, 1994; Pennington and Chavez, 2000), and offshore of MB, coastward of and in the California Current (Collins et al., 2003). NewHorizon06 (NH06; September 2006) and Thompson07 (Th07-1,4; April 2007) occurred in the Pt. Conception upwelling. Thompson07 (Th07-2; April 2007) was west of the California Current in oligotrophic, subtropical gyre water. Sproul05 (Sp05; September 2005) and NewHorizon1307 (NH13-1,2; April 2013) were in the Southern California Bight (SCB), south of Santa Catalina Island and east of San Clemente Island, a region with cyclonic circulation and variable productivity.

The Gatekeeper cruise off Monterey, California had the most intensive and extensive set of measurements (Table 1). The GK-2 deployment was the longest of the cruise, lasting more than 10 d, and is used to develop and illustrate the analysis in this paper. Further information about the deployment is in the results section, as well as in Jackson and Checkley (2011), Petrik et al. (2013), and Dagg et al. (2014).

2.1. LOPC data analysis

We accumulated particle counts in 2-m depth intervals between 2 and 100 m (2–78 m for cruise NH13 unless otherwise noted). We expressed the dependence of concentrations on particle diameter d by calculating number spectra $n(d)$, which are similar to light spectra as a function of wavelength (e.g., Checkley et al., 2008; Jackson and Checkley 2011). The number spectrum was calculated by counting the number of particles ΔN in a small size interval Δd centered on d within a small water volume W: $n(d) = \Delta N/\Delta d\, W$. When calculating n for our data, we increased the value of Δd as d became larger. For any d, the volume of an individual particle V is calculated as for a sphere: $V = (\pi/6)d^3$. The total particle volume concentration between a range of diameters d_l and d_u is

$$C = \int_{d_l}^{d_u} n\, V\, dd = \int_{\ln d_l}^{\ln d_u} n\, V\, d\, d\, \ln(d). \quad (1)$$

where C is a dimensionless concentration, expressing the particle volume as the fraction of the total volume that the particles occupy. Because its value is typically 10^{-6} or less, we frequently multiply it by 10^6 to display the value, indicating this scaling by using units of parts per million (ppm). The first integral in Eq. (1) indicates that the area under a plot of nV versus d is proportional to the volume. Because we are usually interested in a wide range of particle sizes, we usually plot the size distribution as a function of $\ln(d)$ or $\log(d)$. The second integral in Eq. (1) indicates that the area under a curve of nVd versus $\ln(d)$ is also proportional to the total particle volume concentration. We will use nVd to describe the particle volume distribution.

We used the Gaussian fitting procedure in Petrik et al. (2013) to isolate the aggregate fraction, C_a, from the nVd spectrum. The procedure involves fitting a characteristic shape, a Gaussian curve, within the small end of the nVd distribution as a function of $\log d$. The C_a data for each 2 m depth interval were interpolated using linear interpolation to create time series with constant time increments. The time series for each depth had linear trends removed before further time series analysis to remove the influence of long term linear trends on the correlations. There was no smoothing done on the data used for the analyses, although the data shown in Fig. 2 were smoothed for clarity in the display.

We devised a method to isolate groups of falling particles using a cross-correlation procedure to find evidence for a signal moving downward in time. The statistical analysis started with the calculation of cross-correlations between aggregate volumes at different depths for different time offsets (Fig. 3). All correlations calculated for the same combination of depth and time offsets were used to calculate an average c and a standard error for that pair of offsets. A correlation was assumed significant at the 1% confidence level if the absolute value of the mean-to-standard error ratio was greater than 2.58. That is, the null hypothesis was that the mean cross-correlation values were not related, having a normal distribution with a mean of zero.

By using Δz positive or negative, the comparison can be made between upward as well a downward depth offsets. The correlations for upward and downward Δz are similar, but often show a

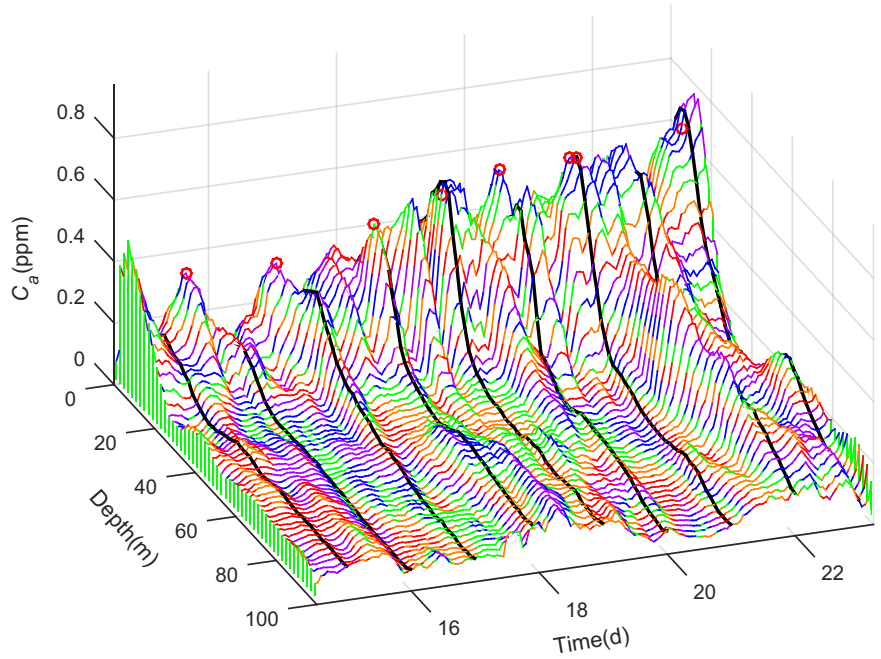

Fig. 2. Depth distribution of aggregate concentration C_a for GK-2 with 2 m depth averaging. For this figure only, the data interpolated to constant time intervals were smoothed with a 4 point moving average filter, first for a given depth, then for a given time. The thick black lines highlight values at midnight local time (PDST). The red circles indicate the daily maximum in C_a. The colors indicate contours of C_a.

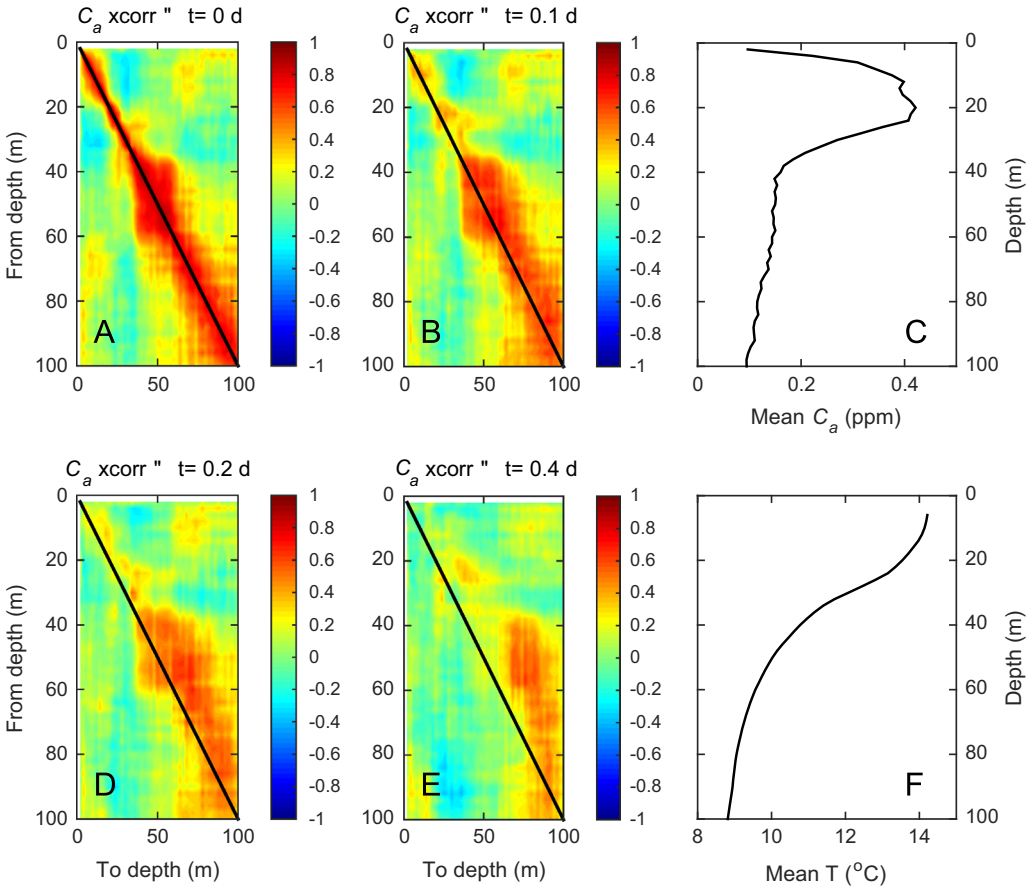

Fig. 3. Cross correlations of aggregate concentrations between different depths for fixed time intervals for GK-2 with 2 m depth binning. Shown are values for time lags of (A) 0; (B) 0.10, (D) 0.20, and (E) 0.40 d. Also shown are the mean (C) aggregate concentration and (F) temperature profiles.

greater correlation downward (Fig. 3). In order to separate out the downward signal, we first calculate what up and down have in common and then subtract the common signal from the original correlations to determine what is different. If Δz and Δt are depth and time offsets, either of which can be positive or negative, and $c(\Delta z, \Delta t)$ is the average correlation between two time series separated by a given Δz with an offset of Δt, then $c(\Delta z,\Delta t)$ can be broken into a *mean* part that is common to positive and negative depth offsets ($m(\Delta z,\Delta t)$) and a downward *bias* that expresses the difference between upward and downward correlations ($b(\Delta z,\Delta t)$):

$$m(\Delta z, \Delta t) = 1/2(c(\Delta z, \Delta t) + c(-\Delta z, \Delta t)) \quad (2)$$

$$b(\Delta z, \Delta t) = 1/2(c(\Delta z, \Delta t) - c(-\Delta z, \Delta t)) \quad (3)$$

The original cross-correlation is just the sum of the two:

$$c(\Delta z, \Delta t) = m(\Delta z, \Delta t) + b(\Delta z, \Delta t) \quad (4)$$

In this notation, the standard minimum depth interval, Δz_1, is 2 m and the standard minimum time offset, Δt_1, is 0.05 d. The motivation for this calculation is discussed further in the results.

2.2. Deployments

We present the results of 12 deployments off the coast of California (Table 1, Fig. 1). The three longest deployments (GK-2, NH13-1, NH13-2) were for ~8 to 12 d. The NH13-1 and -2 deployments had profiles whose maximum depths varied from 78 to 200 m. In order to work with the longest possible time series, the analyses for these two deployments use only the 2–78 m range unless otherwise noted.

3. Results

The distribution of aggregate volume during the GK-2 deployment off Monterey Bay, California, shows the presence of events, where particles move down from the particle maximum (Fig. 2). These events were used previously to determine particle settling rates by calculating the slopes of lines fit by eye to sinking features (Petrik et al., 2013). One such event was between days 21 and 22 (Fig. 2), moving downward from ~25 to 80 m at a velocity of ~55 m d^{-1}. Other events can be seen in days 22–23 and 19–20. There is a more extensive discussion of this in Petrik et al. (2013). By finding and following these events downward, we calculated propagation velocities and their frequency of occurrence.

When the two time series of C_a being correlated have no time lag, the correlations at different depths are highest when the spatial separation between the two is small (Fig. 3A). For GK-2, the region with high correlations extended to separation distances of 20 m in the waters below 50 m, had minimal extent in the region around the particle maximum at 20–30 m, and was slightly higher in the surface 20 m (Fig. 3A). The 5–25 m deep region had the highest aggregate concentrations (Fig. 3C) and extended downward to the base of the thermocline (Fig. 3F). When the time offset between the two sets of time series being correlated is $\Delta t_2 = 0.05$ $d = 1.2$ h, the region with maximum correlations shifts to the right on Fig. 3B, to deeper locations. As the time difference between the two time series increases, the region of maximum correlation moves further to the right on Fig. 3D and E, indicating a movement of particles deeper with more time. This shift in correlation with time is consistent with sinking events.

To focus on the evolution of this vertical shift as a function of time, we averaged all the correlations having the same vertical offset for a given time difference. For example, all the correlations for samples with 1.2 h offset ($\Delta t = 0.05$ d) having paired depths 2 m different (2, 4 m; 4, 6 m; 6, 8 m; …; $\Delta z = 2$ m) had an average (c(2 m, 0.05 d)) and standard deviation calculated. Values of the mean c and its standard deviation were calculated for time offsets from 0 to the shorter of 0.5 d or 1/4 of the total record length and for depth offsets from 0 to 26 m (0–20 m for NH13-1 and NH13-2). The results for GK-2 show highest correlations for the smallest differences in depth and time (Fig. 4A). The correlations up and downward are similar but there are slight differences. As the time difference Δt increases, the depth offset Δz having the highest correlation (largest c) also increases. Again, this is expected for sinking particles.

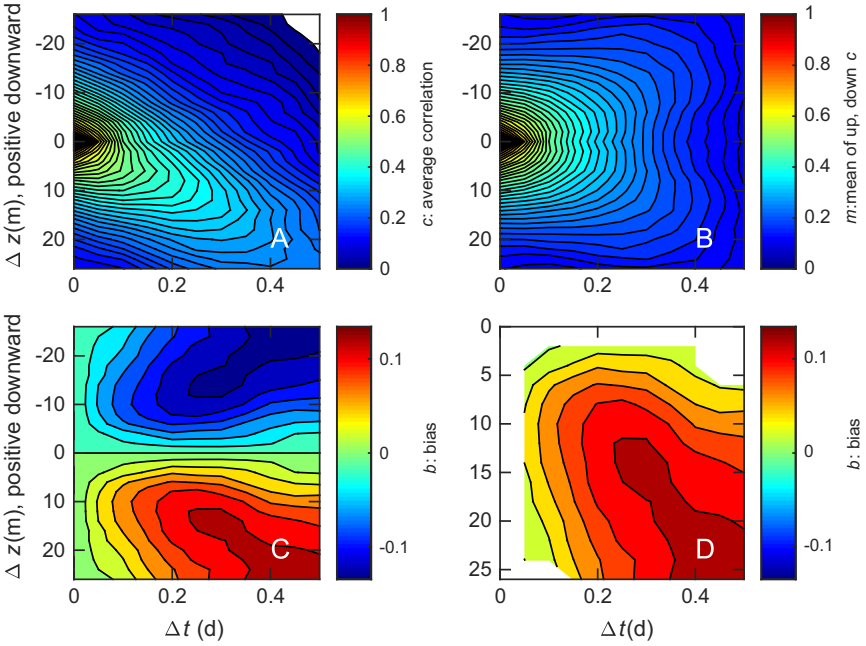

Fig. 4. Mean cross-correlations as a function of time and depth offsets, Δt and Δz for GK-2. Negative depth offsets correspond to depths shallower than the reference depth; positive depth offsets correspond to deeper depths. (A) c, simple cross-correlations; (B) m, average of c for positive and negative Δz; (C) b, difference between up and down correlations divided by 2; (D) as in (C), but with only values for positive Δz and Δt shown. In addition, only values of b statistically significant at the 1% level are included. Of the 130 values of b, 95% were statistically significant at the 1% level. Contour interval is 0.02.

To isolate the vertical offset, we separated the cross-correlations into two parts, one of which is the same up and down, m (Fig. 4B), and one of which contains the differences between the two, b (Fig. 4C). The common part is the mean of the up and down correlations; the difference between the two is the bias. Because the upward differences are the negative of the downward ones ($b(\Delta z,\Delta t) = -b(-\Delta z, \Delta t)$), only the values of the b for positive (downward) depth offsets are shown in subsequent plots (Fig. 4D). In addition, the values of b for zero time are identically zero.

For most of the deployments, those with samples between 0 and 100 m over 2 d or more, there are potentially non-zero offsets for 10 time ($\Delta t = 0.05, 0.10, \ldots, 0.50$ d) and 13 depth ($\Delta z = 2, 4, \ldots, 26$ d) offsets, yielding a total of 130 potentially statistically significant values of b for a deployment. Only those values found statistically significant are shown in these bias graphs.

The bias graph for GK-2 (Fig. 4C and D) has a ridge with a maximum whose depth offset increases with increasing time offsets. This ridge is consistent with a 25 m downward movement of aggregates in about 0.45 d, equivalent to a settling velocity of 56 m d^{-1}. In addition, the width of this high c region spreads out with increasing time differences. Such a spreading could result from multiple particles having different settling velocities.

The existence of a maximum bias region is detectable, although weaker, in about half of the other deployment records (Table 2; Fig. 5). The longest deployments (NH13-1, -2, GK-2) have the greatest fraction of statistically significant biases over the Δt and Δz region used, from 75–95%; the smallest fractions of statistically significant values are only 10-11% for Sp05 and Th07-4. The fraction is small for all the Th07 deployments, 11–25%. This difference between the deployments may result from the greater statistical reliability associated with longer records or may reflect different environmental conditions.

The absolute size of the bias for any deployment varied greatly, with b ranging 0.21 for GK-5 to the small negative values for Th07-2 and −4, $b = -0.05, -0.04$ (Table 2). The GK-5 deployment was in the upwelling region of Monterey Bay and showed signs of rapid aggregation; the Th07-2 and Th07-4 deployments were in relatively oligotrophic environments off Point Conception and in or beyond the California Current. The maximum bias for the three longest deployments, NH13-1, −2, and GK-2, were also low, 0.07–0.13, even though they had among the most extensive pattern of significant biases.

The biases for four of the deployments were mostly negative (3), with three of these (GK-1, Sp05, TH07-4) having the fewest statistically significant b values, $<25\%$, and therefore the least reliable results. Excluding these three, eight of the nine remaining deployments had positive biases, consistent with downward transport of particulate material. The largest biases were generally consistent with downward transport at 30–100 m d^{-1} (Fig. 5).

Table 2
Number of b values possible for a given deployment and the fraction that are statistically significant at the 1% level. Also shown is the b value with the largest magnitude in a deployment. These values correspond to the results shown in 3. The number of possible values is the number of depth offsets times the number of time offsets used ($13 \times 10 = 130$ for GK-2).

Deployment	No. of b values	% Significant values	b at max $\lvert b \rvert$
NH13-1	100	80	0.07
NH13-2	100	79	0.12
GK-1	104	15	−0.10
GK-2	130	95	0.13
GK-3	78	55	0.12
GK-5	78	60	0.21
GK-6	78	49	−0.15
NH06	130	38	−0.08
Sp05	130	10	−0.07
Th07-1	130	25	0.11
Th07-2	130	21	−0.05
Th07-4	130	11	−0.04

3.1. Effect of less frequent sampling

The effect of profiling frequency was examined by increasing the sample interval by factors of 2, 4, and 8, to $\Delta t_1 = 0.1$, 0.2, and 0.4 d (Fig. 6). The general pattern in the contour plot of b, that Δz of the ridge increases for increasing Δt, is visible with the 0.1 and 0.2 d sample intervals. There are fewer of (Δz, Δt) pairs as Δt_1 increases, resulting in decreased resolution for the calculated biases used to make the contour plot. If we estimate a settling velocity of about 45 m d^{-1} from the bias plots in Fig. 6A, the ridge for the first time offset of $\Delta t = 0.4$ d^{-1} should be at $\Delta z = 18$ m, with that for the second offset at 36 m, beyond the 26 m range of this calculation. As a result, there is no ridge possible in the contour plot for the 0.4 d sampling interval in Fig. 6D. Sampling must be done at intervals of 0.2 d or less to resolve episodes of particles sinking at these speeds when the sampling is confined to the upper 100 m.

3.2. Effect of considering a smaller vertical region

Subdividing the water column into 0–50 m and 51–100 m regions for GK-2 before performing the bias calculations yields similar results for the two regions (Fig. 7). For this deployment, the results were consistent through the water column. As noted for the case of less frequent sampling, working with smaller vertical regions does affect the statistical sensitivity by decreasing the sample size for correlations used for the bias calculations, as well as decreasing the maximum settling rate detectable.

3.3. Effect of shorter sampling periods

Dividing the sampling record for GK-2 into four equal periods yields the interesting result that the bias pattern varies from day to day. There is a strong bias pattern in only one of the four periods (Fig. 8D), a weak pattern in a second one (Fig. 8B), and relatively little bias evident during the other two periods (Fig. 8A and C). Dividing the sampling record for NH13-2 gives a similar result, with the strong downward bias evident only in the third quarter (not shown). It is clear that the eye can spot events that are not caught by the analysis.

Further subdividing the records into 1 d periods reveals even more variability for the three longest deployments (Fig. 9), but also results in weaker statistical power. Because of the shorter record length, the value of the longest useful time offset decreases, with the Δt range becoming 0.05 to 0.25 d, rather than the 0.05–0.5 of the longer periods. With fewer time offsets to use, the result is fewer possible number of b values, 65 for GK-2 and 50 for NH13-1 and −2. In addition, with fewer profiles in the shorter records, the statistical power for the correlations was weaker. The number of statistically significant b values varied greatly from day to day, exceeding 5 on 3 of 8 d for GK-2, 2 of 11 d for NH13-1, and 4 of 12 d for NH13-2, for a total of 8 in 31 d, about one quarter of the days. The different number of days with significant b values for NH13-1 and NH13-2 occurred despite the separation between floats being at most 5 km during their simultaneous deployments.

When all of the deployments are considered, there were a total of 48 one-day periods, of which 19 had more than 5 significant b values, about 40% of the days. There was only one deployment, Th07-2, for which none of the three days had any significant values. This was also the deployment in the most oligotrophic waters.

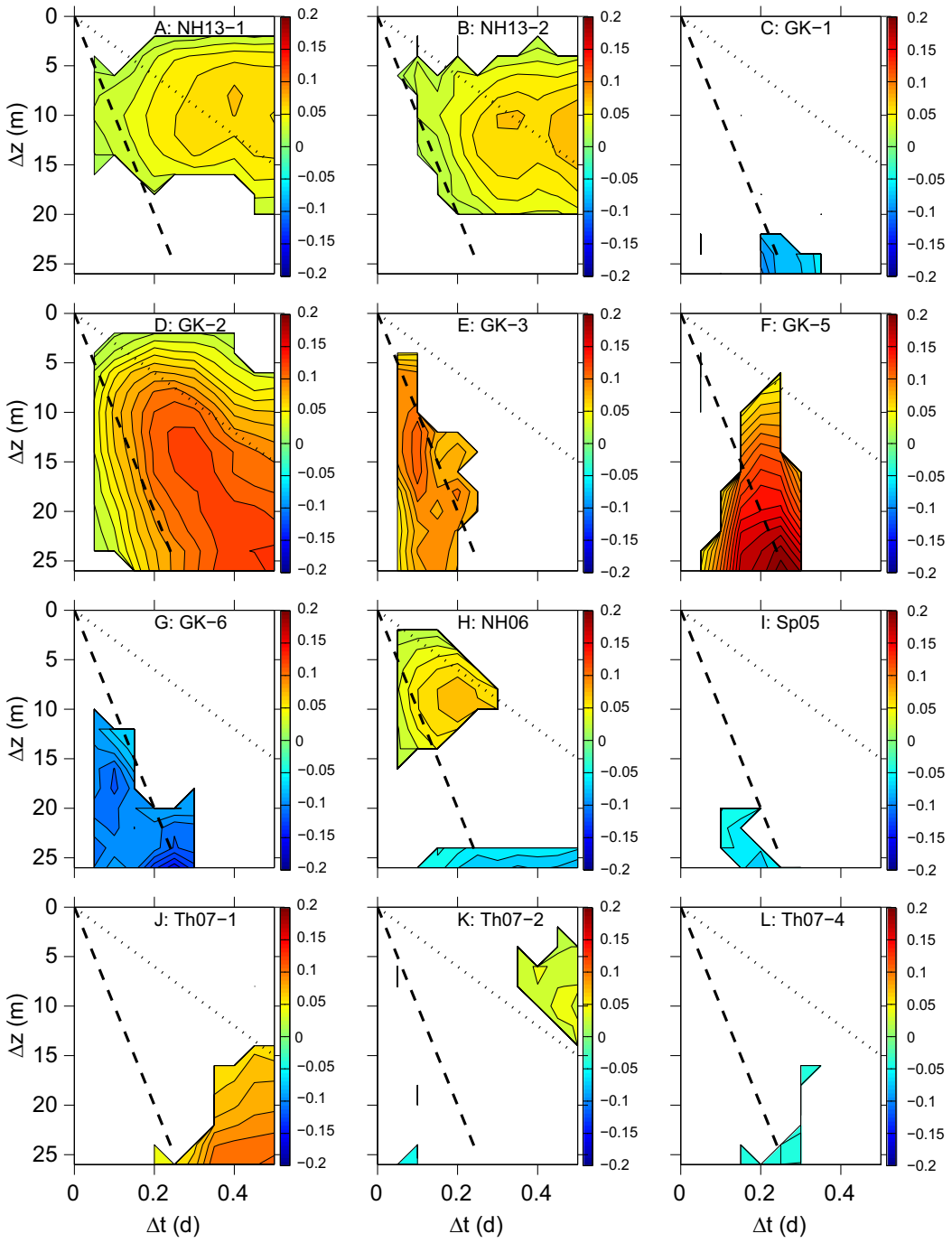

Fig. 5. Mean bias as functions of time and depth offsets (as in Fig. 4D) for deployments noted. The dotted and dashed black lines indicate paths for settling velocity of 30 and 100 m d^{-1}.

3.4. Sinking velocities

We can estimate dominant sinking velocities if we can describe the ridge in the contour plots of b as functions of Δz and Δt (e.g., in Fig. 3D). One way to do this is to choose a value of Δt and find the value of Δz associated with it having the largest positive or smallest negative value of b. The velocity v would then be $v=\Delta z/\Delta t$ for $b>0$ (downward) and $v=-\Delta z/\Delta t$ for $b<0$ (upward). Potential problems with this approach are determining the appropriate value of Δt to use and how to avoid spurious b values. In order to deal with the first issue, we calculate velocities for each potential value of Δt. For the second issue, we argue that for there to be a ridge in b there must be multiple significant b values for the given Δt. We compare velocities calculated only when there are at least 5 values significant of the 13 values possible for a given Δt with velocities calculated with no such condition (Fig. 10).

For the complete set of GK-2 data, the maximum velocity estimate occurs for the shortest offset time and decreases rapidly as the offset time increases. There are 10 offset times with enough significant bs to be suitable for calculating velocities. The velocities vary from 47 to 200 m d^{-1}, with a mean of 75 and a median of 59 m d^{-1}.

The original correlations c used as the starting points for the bias calculation are largest for small values of Δt (Fig. 3A). The bias b is a small signal that must be extracted from the large mean (Fig. 3B). Its values are least for the small Δt. It is not surprising that the variability is largest for the smallest values of Δt.

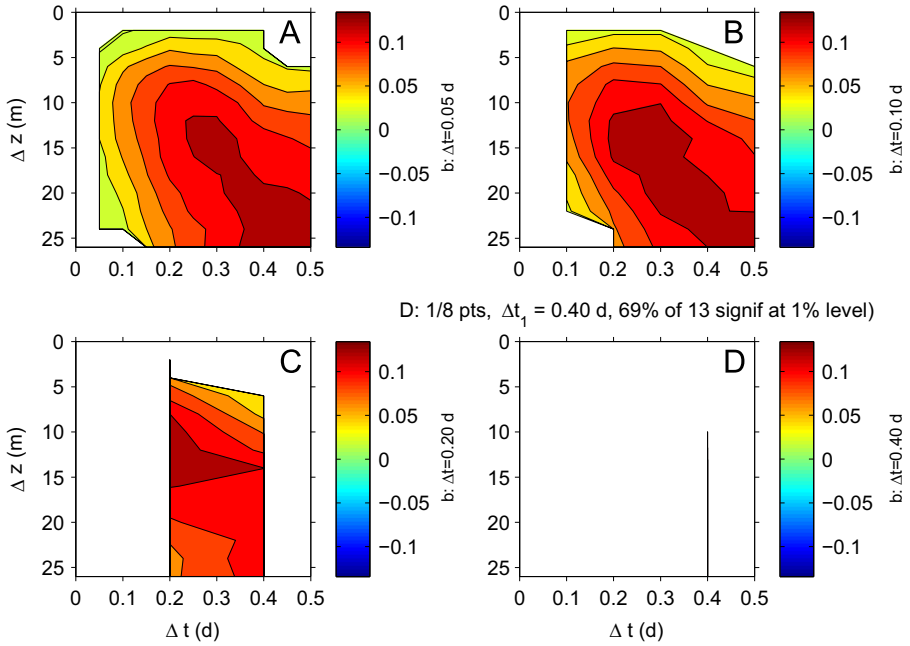

Fig. 6. Effect of increasing sample interval for the same total period of GK-2 on the bias *b*, with the fraction of statistically significant *b* values. (A) The original $\Delta t_1 = 0.05$ d, 95%; (B) $\Delta t_1 = 0.1$ d, 92%; (C) $\Delta t_1 = 0.2$ d, 92%; (D) $\Delta t_1 = 0.4$ d, 69%.

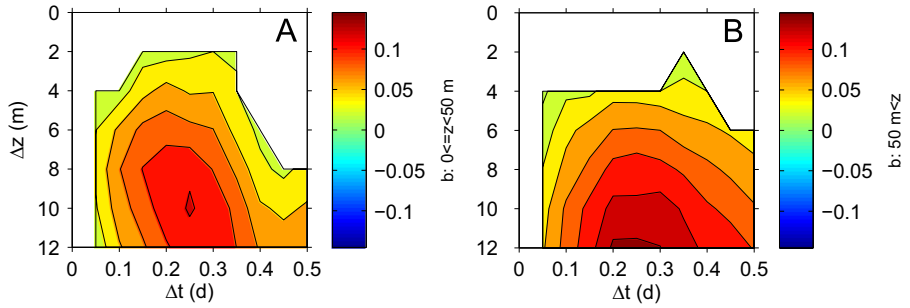

Fig. 7. The calculated bias *b* in GK-2 for the region between left (A) 0–50 m; and right (B) 50–100 m. Note the scale change for the depth offset.

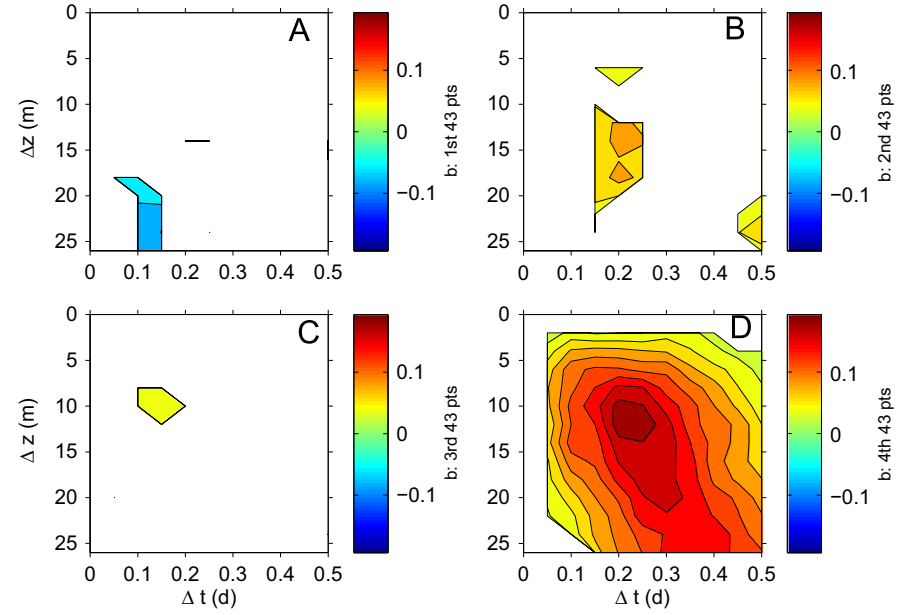

Fig. 8. Effect of dividing the record for GK-2 into four equal parts, each one quarter the original length, on the calculated bias *b*. (A) First quarter; (B) second quarter; (C) third quarter; (D) fourth quarter.

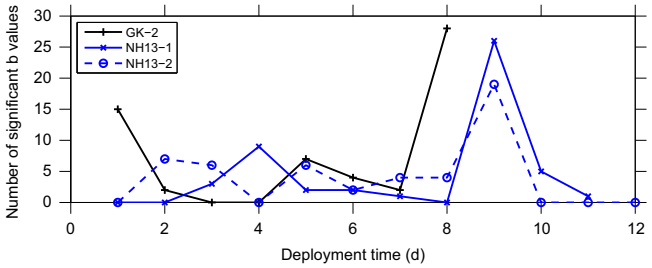

Fig. 9. Number of significant bias values as a function of deployment time for the three longest deployments, GK-2, NH13-1, and NH13-2. The bias calculations were made for each 24 h period. For GK-2, day 0 corresponds to 14 July.

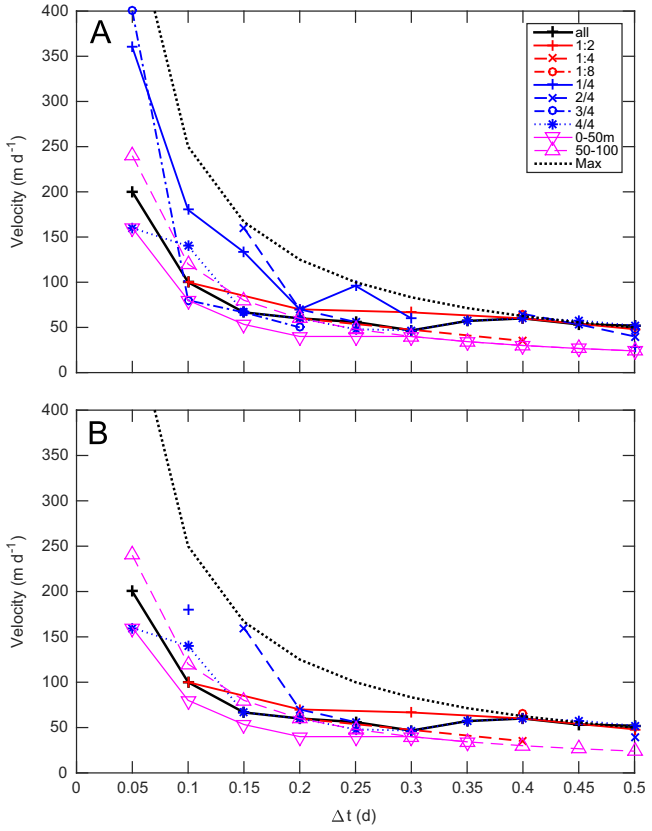

Fig. 10. Velocity estimates for GK-2 at different depth offsets for different data subset calculations. (A) Velocities calculated if there were any significant values of the bias b for a given time offset. (B) Velocities calculated only if there were 5 or more depth offsets with significant values of b for a given time offset. *all* indicates that all points are used for the calculations; 1:2, 1:4, 1:8 indicate that every second, fourth and eighth time points were used; 1/4, 2/4, 3/4, 4/4 indicates that the first, second, third, and fourth time fraction were used; 0–50 m and 50–100 indicates that only the upper 50 m and 50–100 m samples were used. The dotted lines indicate the maximum possible velocities that can be calculated.

The estimated velocities for GK-2 decrease from Δt values from 0.05 to 0.15 d, stabilize around 50–70 m d^{-1} between Δt from 0.15 to 0.35 d, and then decrease with increasing Δt as the estimated velocity essentially equals the maximum possible velocity. The maximum velocity possible, here equal to the maximum possible depth offset 25 m divided by Δt, decreases with increasing Δt (e.g., Fig. 10).

The different subsets of the GK-2 datasets show the same general pattern (Fig. 10). The highest velocities, more than 400 m d^{-1}, were for two of the values calculated on the quarter length records when there was no requirement for a minimum number of significant maximum biases (Fig. 10A). Imposing the minimum requirement of 5 significant b values for a given Δt decreases the maximum velocity to about 250 m d^{-1}, as well as reducing the number of anomalously high values (Fig. 10B).

Table 3
Estimated settling velocities for different deployments. Shown are the number of time offset intervals with more than four depths having significant biases at the 1% significance level for velocity estimates (no. of v) and the minimum, maximum, mean and median velocities and their standard deviation of those estimates. The largest possible value for no. of v is 5, corresponding to Δt=0.15, 0.10,…,0.35 d.

Deployment		Velocities(m/d)				
	No. of v	Min	Max.	Mean	Median	std
NH13-1	5	29	67	47	48	14
NH13-2	5	29	67	45	48	15
GK-1	0	–	–	–	–	–
GK-2	5	47	67	57	57	7
GK-3	2	90	160	125	125	49
GK-5	4	87	173	123	117	37
GK-6	2	−80	−60	−70	−70	14
NH06	3	40	53	44	40	8
Sp05	0	–	–	–	–	–
Th07-1	1	–	–	74	–	–
Th07-2	0	–	–	–	–	–
Th07-4	1	–	–	−80	–	–

Again, the pattern is similar for the other deployments, although most do not have as large a number of Δt values meeting the minimum requirement of 5 significant b values for $0.15 \le \Delta t \le 0.35$ d (Table 3). If we use the velocities in this region of relative stability in Fig. 10, the smallest positive mean velocities were for three deployments in the Southern California Bight (NH06, NH13-1, NH13-2), 44–47 m d^{-1}; the largest were for deployments among newly formed aggregates during an algal bloom in Monterey Bay (Gk-3, GK-5) 123–125 m d^{-1} (Table 3). The three longest deployments (NH13-1, NH13-2, and GK-2) had much smaller median velocities, ranging from 33 to 51 m d^{-1}. GK-6 went against the downward movement, with calculated upward velocities having a mean of −70 m d^{-1}, as did the one value for Th07-4, −80 m d^{-1}.

4. Discussion

This analysis of time-dependent distribution and abundance of aggregates has revealed at least two aspects of particle settling in the near-surface ocean. The first is the range of aggregate settling velocities; the second is the episodic nature of particle sinking.

4.1. Sinking rates

Many estimates of particle sinking rates have used in situ measurements of velocities for marine snow particles: Alldredge and Gotschalk (1988) measured rates of 10–200 m d^{-1} at scuba diving depths, with the values centered at about 60 m d^{-1}; Shanks and Trent (1980) measured velocities equal to 43–95 m d^{-1}, also within scuba diving depth range. Pilskaln et al. (1998) used a remotely operated vehicle (ROV) to observe aggregate sinking deeper, from 100 to 500 m, observing mean sinking rates of 16–25 m d^{-1}. All of the above were off California. Elsewhere, Asper (1987) measured rates of 1–36 m d^{-1} at 380 m in Panama Basin by using a remote camera system; Diercks and Asper (1997) deployed the camera system at 167 m depth in the Gulf of Mexico, measuring rates of 10–80 m d^{-1}, and in the Black Sea 688 m deep, finding rates of 1–300 m d^{-1}. The mean settling velocities calculated here ranged from 44–125 m d^{-1}, aside from two instances with an upward velocity (Table 3). Thus, the SOLOPC observations are consistent with these published observations, particularly the previous deployments made in surface waters off California.

4.2. Effectiveness of sampling strategy

The use of high frequency, high spatial resolution measurements provided by the SOLOPC opens up new possibilities for exploring particle dynamics. However, there are constraints to velocities that can be measured, many of which depend on the sampling strategy. Important variables include the length of the deployment as well as the minimum depth and time resolutions.

Because longer records provide more samples, they improve the accuracy of the correlation calculation and, hence, the bias value. As a result, the bias value required to give a significant result should decrease for longer records. Thus, deployments of different lengths are not strictly comparable. Another constraint is that the bias signal must be extracted from the correlation signal that is much larger, particularly for small offsets in time and space (e.g., Fig. 3). The largest values of the bias typically are for $\Delta t > 0.2$ d (Fig. 3). Deployments that are too short must also contend with this factor.

The largest bias that we observed was for GK-5, in an upwelling area in which there were signs of aggregate formation. This was also one of the shorter deployments. NH13-1 and NH13-2 had small maximum biases, but the longer records made it possible to extract velocity estimates. The small bias limitation can be seen for Th07-2 and Th07-4, in oligotrophic conditions where there was not enough of a signal to estimate a settling velocity and the deployments were 3.46 and 4.13 d. It is possible that the lower particle concentrations in oligotrophic regions result in slower aggregation rates and result in fewer episodes of flux than in eutrophic regions, but longer deployments are needed to establish such a different temporal pattern.

In addition, the sampling intervals constrain the range of velocities that can be calculated, even with perfect bias estimates. The maximum velocity equals the maximum depth offset divided by the minimum time offset, here $v_{max} = \Delta z_{max}/\Delta t_1 = 26$ m/0.05 $d = 520$ m d^{-1}. Similarly, the minimum velocity is the minimum depth offset divided by the maximum time offset, here $v_{min} = \Delta z_1/\Delta t_{max} = 2$ m/0.5 $d = 4$ m d^{-1}. Increasing the sample interval, such as by a factor of 8, decreases the maximum measurable velocity to 65 m d^{-1}.

Thus, statistical problems with detecting bias among the correlations for small time and depth intervals also effectively decrease the range of velocities it is possible to detect. To capture particle settling with velocities less than the 100 m d^{-1} that is usually reported for near surface aggregates requires a sampling interval no more than about 0.25 d.

Lastly, the method depends on variability in export. In a system at steady state, there would be no events to track.

As the opportunities for observing particle sedimentation with profiling floats and gliders an increase, the choices of sampling strategy will play an important role in observable sedimentation, in observing sporadic events as well as their spatial extent.

4.3. Episodic nature of settling events

Also striking about the deployment results is how episodic the sedimentation events are. The longer deployments show aggregate export in about one quarter of the days.

There was only one example of upward aggregate movement, for GK-6. This may represent buoyant particles, such as observed by Riebesell (1992) or may represent movement of water. In either case, this was for a short deployment.

The fact that NH13-1 and 2 had differences in their event histories despite being within 5 km of each during their deployments implies that export was not simply controlled by large-scale physics, such as wind forcing. Further evidence comes from the lack of a clear relationship between winds at observing station M2 in Monterey Bay and the sedimentation pulses in GK-2 (not shown).

There was a tendency for particle maxima to occur at night. For observations smoothed as in Fig. 2, the aggregate maxima occurred in the 12 h centered around local midnight for 7 of 8 days during GK-2 (Fig. 2), 6 of 10 during NH13-1, and 8 of 12 during NH 13-2. However, we were unable to relate mean or maximum particle concentration over a 1 d period to the number of significant biases shown in Fig. 9 (not shown). This lack of a relationship suggests that episodic flux events were not driven simply by aggregate concentrations.

Complicating the data interpretation is the fact that the profiling floats are only semi-Lagrangian, as they can change water masses with time. This was particularly true for GK-2, which initially moved offshore before encountering the California Current (Fig. 1), with clearly observable changes in water mass properties (e.g., Fig. 5 in Petrik et al., 2013). Whether the episodic nature of the flux is purely temporal or a mixture of temporal and spatial, it is observable variability that is episodic.

High temporal variability is a hallmark of sedimentation in the ocean. For example, Jouandet et al. (2014) observed the formation and abrupt sedimentation of phytoplankton aggregates over a period of two days in the surface mixed layer off the Kerguelen Islands. Deeper, Marty et al. (2009) measured sediment trap fluxes near the DYFAMED site in the western Mediterranean Sea at 200 m with 6 h resolution. In both the Kerguelen and Mediterranean studies, rapid changes in the carbon flux were not associated with large inputs of nutrients to surface waters. Marty et al. (2009) argued that changes in ecosystem processes, including grazing, in the overlying waters were responsible for the variability. In the same depth range, Lampitt et al. (1993) monitored particle sizes at 270 m depth, observing diel patterns in sedimentation. Observations of sedimentation events and high variability extend to the deep ocean (e.g. Conte et al., 2001; Conte and Weber, 2014) and the benthos (Billett et al., 1983; Baldwin et al., 1998).

4.4. What this tells us about particle transport in the ocean

While the bias approach to observing export events does not capture the constant flux, the low aggregate concentrations around 100 m suggest that it must be relatively small at those depths. The questions become “what keeps the particles in high concentration from falling out of the surface layer”, “what allows the export events?” and “how widespread are they?”

Aggregates are relatively amorphous particles, often formed by coagulation processes (e.g., Jackson, 1995, 2005; Jouandet et al., 2014). Such processes are always occurring but their rates are very sensitive to changes in particle concentration and stickiness. Another class of falling particles, fecal pellets, is formed as part of zooplankton feeding on particles, including aggregates. There is extensive documentation that animals, including copepods and euphausiids, consume aggregates (e.g., Shanks and Edmondson, 1990; Shanks and Walters, 1997; Dilling et al., 1998; Koski et al., 2005). Such feeding converts falling aggregates to falling pellets, increasing sinking speed while decreasing the flux by the amount of material assimilated by the animals.

In addition to aggregate export being driven by aggregate formation and settling, export can be controlled by consumption of sinking particles. Such a mechanism has been called the “retention filter” (Wexels Riser et al., 2007) and the “gatekeeper” hypothesis (Jackson and Checkley, 2011). Near the surface, high concentrations of the primary particles, such as algae, fuel the formation of aggregates. Aggregates fall into regions of lower particle concentrations, where the coagulation rates drop dramatically, cutting off the formation of new aggregates but still allowing the consumption of aggregates and their conversion to fewer but faster falling fecal pellets. Any change in zooplankton

feeding pressure, as might occur with changes in zooplankton concentrations associated with patchiness or diel vertical migration, would result in changes in export.

Microbes are also organic matter consumers that could influence the flux. However, microbial metabolism of aggregates typically consumes about 10% of the mass per day (Ploug and Grossart, 2000), which at settling rates of 50 m d^{-1} would decrease the aggregate mass by only 20% while particles fall through the upper 100 m. Even if the microbes were controlling the flux in the upper 100 m, there still needs to be a mechanism yielding large changes in microbial activity over a few days. Either reason suggests that microbes are not responsible for the variability.

The average sinking velocity can also be estimated from the particle size distribution after assuming a relationship between the size and sinking velocity (e.g., Checkley et al., 2008). Calculations made using the aggregate size distributions for the GK deployments and assumed density relationships yielded average velocities 22–54 m d^{-1}, with the highest velocity associated with GK-4 (Petrik et al., 2013). Again, the results for the different methods are consistent.

The previously published techniques for measuring particle sinking velocities cited above provide the rates for individual particles. They demonstrate that there is large variation in settling rate, some of it related to particle size. As a result, we do not expect a single velocity to characterize the falling particle field. The mean bias field (e.g., Fig. 3) usually includes more than one significant depth offset at a given time offset, forming a spread of values decreasing with increasing distance from the optimal depth offset. Such a spread would be produced by a range of particle settling rates. The effect of such a velocity distribution on arrival times was noted by Lampitt et al. (1993) for observations at 270 m in the North Atlantic Ocean.

5. Conclusions

The SOLOPC profiling float system provides a powerful tool to study particle dynamics in the upper 100–200 m of the water column with high temporal and spatial resolution. The particle profiling measurements provide a needed tool to study the dynamics of carbon export in the surface region where traditional measurements associated with sediment traps do not work well (e.g., Buesseler et al., 2007). This region is particularly important because it is the region of the water column where most of the flux exported from the euphotic zone disappears (e.g. Martin et al., 1987). Our observations highlight the importance of episodic events on times scales of a day or less on the export of organic carbon downward from the near-surface region.

Acknowledgements

This work was supported by U.S. National Science Foundation (NSF) awards OCE-0927863 to GJ, OCE-0928139 to MD, and OCE-0928425 to DC.

References

Alldredge, A.L., Gotschalk, C., 1988. In situ settling behavior of marine snow. Limnol. Oceanogr. 33, 339–351.
Alldredge, A.L., Gotschalk, C., 1989. Direct observations of the mass flocculation of diatom blooms: characteristics, settling velocities and formation of diatom aggregates. Deep-Sea Res. 36, 159–171.
Asper, V.L., 1987. Measuring the flux and sinking speed of marine snow aggregates. Deep-Sea Res. 34, 1–17.
Baldwin, R.J., Glatts, R.C., Smith Jr., K.L., 1998. Particulate matter fluxes in the benthic boundary layer at a long time-series station in the abyssal NE Pacific: composition and fluxes. Deep-Sea Res. II 45, 643–665.
Billett, D.S.M., Lampitt, R.S., Rice, A.L., Mantoura, R.F.C., 1983. Seasonal sedimentation of phytoplankton to the deep-sea benthos. Nature 302, 520–522.
Breaker, L.C., Broenkow, W.W., 1994. The circulation of Monterey Bay and related processes. Oceanogr. Mar. Biol. 32, 1–64.
Briggs, N., Perry, M.J., Cetinic, I., Lee, C., D'Asaro, E., Gray, A.M., Rehm, E., 2011. High resolution observations of aggregate flux during a sub-polar North Atlantic spring bloom. Deep-Sea Res. I 58, 1031–1039.
Buesseler, K.O., Antia, A.N., Chen, M., Fowler, S.W., Gardner, W.D., Gustafsson, O., Harada, K., Michaels, A.F., van der Loeff, M.R., Sarin, M., Steinberg, D.K., Trull, T., 2007. An assessment of the use of sediment traps for estimating upper ocean particle fluxes. J. Mar. Res. 65, 345–416.
Checkley, D.M., Barth, J.A., 2009. Patterns and processes in the California Current System. Prog. Oceanogr. 83 (1-4), 49–64. http://dx.doi.org/10.1016/j.pocean.2009.07.028.
Checkley Jr., D.M., Davis, R.E., Herman, A.W., Jackson, G.A., Beanlands, B., Regier, L.A., 2008. Assessing plankton and other particles in situ with the SOLOPC. Limnol. Oceanogr. 53, 2123–2136.
Collins, C.A., Pennington, J.T., Castro, C.G., Rago, T.A., Chavez, F.P., 2003. The California Current system off Monterey, California: physical and biological coupling. Deep-Sea Res. II 50 (14–16), 2389–2404. http://dx.doi.org/10.1016/s0967-0645(03)00134-6.
Conte, M.H., Ralph, N., Ross, E.H., 2001. Seasonal and interannual variability in deep ocean particle fluxes at the Oceanic Flux Program (OFP)/Bermuda Atlantic Time Series (BATS) site in the western Sargasso Sea near Bermuda. Deep-Sea Res. 48, 1471–1505.
Conte, M.H., Weber, J.C., 2014. Particle flux in the deep Sargasso Sea: the 35-year Oceanic Flux Program time series. Oceanography 27 (1), 142–147.
Dagg, M., Jackson, G.A., Checkley Jr., D.M., 2014. The distribution and vertical flux of fecal pellets from large zooplankton in Monterey Bay and coastal California. Deep-Sea Res. I 94, 72–86.
Dall'Olmo, G., Mork, K.A., 2014. Carbon export by small particles in the Norwegian Sea. Geophys. Res. Lett. 41, 2921–2927.
Diercks, A.R., Asper, V.L., 1997. In situ settling speeds of marine snow aggregates below the mixed layer: Black Sea and Gulf of Mexico. Deep-Sea Research I 44, 385–398.
Dilling, L., Wilson, J., Steinberg, D., Alldredge, A.L., 1998. Feeding by the euphausiid *Euphausia pacifica* and the copepod *Calanus pacificus* on marine snow. Mar. Ecol. Prog. Ser. 170, 189–201.
Herman, A.W., Beanlands, B., Phillips, E.F., 2004. The next generation of optical plankton counter: the laser-OPC. J. Plank. Res. 26, 1135–1145.
Jackson, G.A., 1995. Comparing observed changes in particle size spectra with those predicted using coagulation theory. Deep-Sea Res. II 42, 159–184.
Jackson, G.A., 2005. Coagulation theory and models of oceanic plankton In: Droppo, I., Leppard, G., Liss, S., Milligan, T. (Eds.), Flocculation in Natural and Engineered Environmental Systems. CRC Press, Boca Raton, FL, pp. 271–292.
Jackson, G.A., Checkley Jr., D.M., 2011. Particle distributions in the upper 100 m water column and their implications for animal feeding in the plankton. Deep-Sea Res. I 58, 283–297.
Jouandet, M.-P., Jackson, G.A., Carlotti, F., Picheral, M., Stemmann, L., Blain, S., 2014. Rapid formation of large aggregates during the spring bloom of Kerguelen Island: observations and model comparisons. Biogeosciences 11, 4353–4406.
Koski, M., Kiørboe, T., Takahashi, K., 2005. Benthic life in the pelagic: aggregate encounter and degradation rates by harpacticoid copepods. Limnol. Oceanogr. 50 (1254-163).
Lampitt, R.S., Hillier, W.R., Challenor, P.G., 1993. Seasonal and diel variation in the open ocean concentration of marine snow aggregates. Nature 362, 737–739.
Martin, J.H., Knauer, G.A., Karl, D.M., Broenkow, W.W., 1987. VERTEX: carbon cycling in the northeast Pacific. Deep-Sea Res. 34, 267–285.
Marty, J.C., Goutx, M., Guigue, C., Leblond, N., Raimbault, P., 2009. Short-term changes in particulate fluxes measured by drifting sediment traps during end summer oligotrophic regime in the NW Mediterranean Sea. Biogeosciences 6, 87–899.
Pennington, J.T., Chavez, F.P., 2000. Seasonal fluctuations of temperature, salinity, nitrate, chlorophyll and primary production at station H3/M1 over 1989–1996 in Monterey Bay, California. Deep-Sea Res. II 47 (5-6), 947–973.
Petrik, C.M., Jackson, G.A., Checkley Jr., D.M., 2013. Aggregates and their distributions determined from LOPC observations made using an autonomous profiling float. Deep-Sea Research I 74, 64–81.
Pilskaln, C.H., Lehmann, C., Paduan, J.B., Silver, M.W., 1998. Spatial and temporal dynamics in marine aggregate abundance, sinking rate and flux: Monterey Bay, central California. Deep-Sea Res. II 45, 1803–1837.
Ploug, H., Grossart, H.-P., 2000. Bacterial growth and grazing on diatom aggregates: respiratory carbon turnover as a function of aggregate size and sinking velocity. Limnol. Oceanogr. 45, 1467–1475.
Ploug, H., Iversen, M.H., Fischer, G., 2008. Ballast, sinking velocity, and apparent diffusivity within marine snow and zooplankton fecal pellets: implications for substrate turnover by attached bacteria. Limnol. Oceanogr. 53 (5), 1878–1886.
Riebesell, U., 1992. The formation of large marine snow and its sustained residence in surface waters. Limnol. Oceanogr. 37, 63–76.
Rykaczewski, R.R., Checkley, D.M., 2008. Influence of ocean winds on the pelagic ecosystem in upwelling regions. PNAS 105, 1965–1970. http://dx.doi.org/10.1073/pnas.0711777105|ISSN 0027-8424.

Shanks, A.L., Trent, J.D., 1980. Marine snow: sinking rates and potential role in vertical flux. Deep-Sea Res. 27, 137–144.
Shanks, A.L., Edmondson, E.W., 1990. The vertical flux of metazoans (holoplankton, meiofauna, and larval invertebrates) due to their association with marine snow. Limnol. Oceanogr. 35, 455–463.
Shanks, A.L., Walters, K., 1997. Holoplankton, meroplankton, and meiofauna associated with marine snow. Mar. Ecol. Prog. Ser. 156, 75–86.
Turner, J.T., 2014. Zooplankton fecal pellets, marine snow, phytodetritus and the ocean's biological pump. Prog. Oceanogr. , http://dx.doi.org/10.1016/j.pocean.2014.08.
Wexels Riser, C., Reigstad, M., Wassmann, P., Arashkevich, E., Falk-Petersen, S., 2007. Export or retention? Copepod abundance, faecal pellet production and vertical flux in the marginal ice zone through snap shots from the northern Barents Sea. Polar Biol. 30, 719–730.